universe

MDPI

Article

CLASH-VLT: The Fifth Force in Chameleon Gravity from Joint Lensing and Kinematics Cluster Mass Profiles

Lorenzo Pizzuti [1,2,*], Federico Rivano [1], Keiichi Umetsu [3] and Andrea Biviano [2,4]

[1] Dipartimento di Fisica G. Occhialini, Università di Milano-Bicocca, Piazza della Scienza 3, 20126 Milano, Italy; f.rivano@campus.unimib.it
[2] INAF-Osservatorio Astronomico di Trieste, Via G. Tiepolo 11, 34143 Trieste, Italy; andrea.biviano@inaf.it
[3] Academia Sinica Institute of Astronomy and Astrophysics (ASIAA), No. 1, Section 4, Roosevelt Road, Taipei 106216, Taiwan; keiichi@asiaa.sinica.edu.tw
[4] IFPU—Institute for Fundamental Physics of the Universe, Via Beirut 2, 34014 Trieste, Italy
* Correspondence: lorenzo.pizzuti@unimib.it

Abstract

We present a high-precision joint gravitational-lensing and kinematic analysis of nine massive galaxy clusters from the CLASH and CLASH-VLT surveys to test chameleon screening gravity and its $f(R)$ sub-class at Mpc scales. We investigate the dependence on the assumed parametrization of the total cluster mass profile by adopting three models, namely Navarro–Frenk–White (NFW), Burkert, and Hernquist. When cuspy models (NFW or Hernquist) are assumed in the general chameleon framework, the combined constraints from the nine clusters are fully consistent with General Relativity (GR), excluding large regions of the modified-gravity parameter space (the coupling constant $\mathcal{Q}$ and the background chameleon field ϕ_∞), providing one of the tightest bounds on general chameleon models with clusters to date. In contrast, adopting a Burkert profile—disfavored by lensing data—leads to a mild ($\sim 2\sigma$) departure from the GR expectation in joint analysis. When considering the $f(R)$ sub-case, we obtain a bound on the background scalaron field of $|f_R| \lesssim 2-5\times10^{-5}$ (95% C.L.) for NFW and Hernquist models, in agreement with current constraints at cosmological scales, and an apparent deviation from standard gravity of $\log_{10}|f_R| = -4.7\pm1.2$ for the Burkert case. We investigate the impact of systematics in the kinematical analysis, showing that the tension is mitigated when clusters exhibiting clear dynamical disturbance are excluded from the sample. Our results show that galaxy clusters provide competitive tests of screened modified gravity at mega-parsec scales, while highlighting the critical role of accurate mass modeling and dynamical-state assessment. The upcoming generation of wide-field lensing surveys and spectroscopic follow-up programs will enable similar analyses on substantially larger samples, offering the prospect of tightening cluster-based constraints on gravity and the dark sector.

Keywords: galaxy clusters; kinematics; dark energy; modified gravity

Academic Editors: Lorenzo Iorio and Øyvind Grøn

Received: 7 March 2026
Revised: 13 April 2026
Accepted: 24 April 2026
Published: 26 April 2026

1. Introduction

Since its discovery, the origin of the low-redshift accelerated expansion of the Universe [1,2] has became one of the fundamental open questions in cosmology. In the current cosmological paradigm, formalized by the so-called ΛCDM model, this acceleration arises from a cosmological constant, Λ, in Einstein's field equations of General Relativity (GR, hereafter), for which standard physics has found no natural explanation (e.g., [3,4]). In the simplest interpretation, the cosmological constant encapsulates the contribution of a new

unknown component accounting for ∼68% of the energy budget of the universe [5], dark energy (DE) [6], characterized by a constant equation of state $p_\Lambda = w\rho_\Lambda$, with $w = -1$.

While the ΛCDM model remarkably describes a large variety of phenomena across different scales, the increase in the quality and quantity of datasets has highlighted several tensions between early and late time observations (see, e.g., [7,8]). In addition, recent DESI results [9] have provided evidence in favor of a dynamical DE evolving with cosmic time $w = w(z)$, lowering the efficacy of the ΛCDM model even more and suggesting the need for some modification. However, more recent Bayesian studies [10] have shown that DESI DR2's deviation from ΛCDM is largely driven by inter-dataset tensions, and it may be reduced once residual systematic effects are properly accounted for. This highlights the subtle interplay among systematics, dataset consistency, and theoretical modeling when testing non-standard cosmological scenarios.

Among the various possibilities, a large-scale remodeling of the gravitational interaction (i.e., modifying GR) is also being taken in consideration. While GR has been tested with enormous success on small scales [11–13], modifications at a cosmological level may still be viable and provide a phenomenology which mimics the background evolution of the ΛCDM paradigm [14,15]. Both dark sector and modified gravity (MG) alternatives change the formation and evolution of cosmic structures through the introduction of new (dynamical) degrees of freedom. In this regard, galaxy clusters emerge as exceptional laboratories to constrain the ΛCDM framework [16] and possible signatures of new physics at a cosmological level [17–19]. In fact, they are the largest and most massive self-gravitating systems in the universe, constituting the endpoint of the structure formation process [20].

The internal shape of a cluster and the distribution of both baryonic and dark matter carry pivotal information on the nature of gravity and of the dark sector [21,22]. Indeed, MG or new dynamical components change the relation between matter perturbation and gravitational potentials. Non-relativistic (galaxies and gas) and relativistic (photons) tracers of the mass profile respond differently to gravitational interaction if GR is modified; thus, joint analyses combining lensing [23] and kinematics [24] mass reconstruction can be used to constrain MG models at Mpc scales. Since GR predictions fit Solar System and galactic tests almost perfectly, in order to preserve their efficacy, viable MG theories need to implement a screening mechanism [25–27], which suppresses the new degrees of freedom and restores standard gravity at small scales. The details of the screening—namely how efficiently the suppression is achieved —determine the resulting phenomenology, imprinting distinctive signatures on the mass distribution and dynamical properties of galaxy clusters (e.g., [28]).

In this work, we focus on the popular chameleon screening theories [29–31]—a branch of scalar–tensor theories of gravity—where the new degree of freedom generates a fifth force affecting the motion of non-relativistic particles, which depends on the matter density itself. If appropriately tuned, in high-density regions the resulting effective mass of the chameleon field becomes so large that the fifth-force results are negligible and GR is re-established. The strength of the modification depends on the background value of the chameleon field ϕ_∞ and the coupling with matter $\mathcal{Q}$. A widely studied sub-class of chameleon models is the $f(R)$ gravity [32,33]. In this framework the Einstein–Hilbert action is generalized, introducing a function of the Ricci scalar, $f(R)$. As a result, the geometry of spacetime is modified, and an additional fifth force is mediated by the scalaron field, $f_R = \partial f/\partial R$, which can be mapped onto the chameleon field. A large number of stringent constraints has been obtained for both general chameleon models and specific $f(R)$ realizations across a wide range of physical scales [34–40].

Recent works have further explored general screened modified gravity using strong-lensing observables on galactic and sub-galactic scales. In particular, ref. [41] introduced a phenomenological parametrization of MG in terms of a post-Newtonian slip parameter $\gamma_{\rm PN}$

and a screening scale Λ, modeling the transition from GR to a modified regime as a sharp change in the relation between the metric potentials. Using time delays in strong lenses, they obtained constraints of the form $|\gamma_{\rm PN} - 1| \lesssim 0.2\,(\Lambda/100\,{\rm kpc})$, effectively probing scales in the range $\Lambda \sim$ 10–200 kpc. Similar approaches have been adopted in galaxy-scale analyses combining strong lensing and stellar dynamics to constrain deviations from GR in a largely phenomenological framework (e.g., [42]).

More recently, strong lensing of gravitational waves has been proposed as a novel probe of screened MG models by constraining $\gamma_{\rm PN}$ (e.g., [43]). These analyses provide a new window on gravity at large scales, being sensitive to the relativistic sector and to the behavior of gravitational waves across cosmological distances.

These approaches are complementary to the present work, but conceptually different. First, chameleon-like theories are characterized by a screening mechanism that depends primarily on the local gravitational potential (or density), rather than on a fixed physical scale. In this case, the transition between screened and unscreened regimes can be associated with an effective screening radius S, defined implicitly by the structure of the density field, typically of $\mathcal{O}({\rm Mpc})$, making possible deviations hard to detect in galactic environments. In this regard, galaxy clusters remain a particularly interesting regime to explore; they lay at the interface between astrophysics and cosmology, where screening mechanisms may operate in a non-trivial and potentially observable way, leaving characteristic imprints on cluster mass profiles. Second, while strong-lensing analyses probe the relativistic sector typically on galaxy scales, the analysis presented in this work exploits a joint comparison between relativistic (strong and weak lensing) and non-relativistic (galaxy kinematics) tracers at Mpc scales. This allows us to directly constrain the physical parameters of chameleon gravity, namely the coupling $\mathcal{Q}$ and the background field value ϕ_∞, extending existing constraints to environments where the chameleon mechanism is expected to operate differently due to the diverse densities and potentials involved.

Moreover, despite its relative simplicity, chameleon gravity provides a controlled yet versatile theoretical framework that makes it an interesting case study to fully exploit the constraining power of clusters, and to develop methodologies that can later be extended to more complex MG scenarios.

In the following, we use high precision gravitational lensing and member galaxies' kinematical information of nine massive galaxy clusters, extensively studied within the CLASH [44] and CLASH-VLT [45] collaborations, in order to constrain the general chameleon gravity and the sub-class of $f(R)$ models. By means of the MG-MAMPOSST code [46], we obtain the joint lensing-kinematics posterior distributions of the free parameters describing the chameleon model to constrain the allowed region of the parameter space. Since the efficiency of the chameleon screening is strongly related to the structure of the matter distribution, we explore how different prescriptions of the total cluster mass profile affect the results. This follows from the theoretical analysis performed in [47], where we implemented semi-analytical solutions of chameleon gravity for different mass ansatze and we validated them against simulated halos; here, we apply such a framework to real cluster datasets for the first time. We further discuss the impact of systematics, in particular deviation dynamical relaxation and the presence of substructures in the distribution of the member galaxies.

This paper is structured as follows: in Section 2 we provide a brief overview of the chameleon model; in Section 3 we present the dataset and the methodology used for the analysis before presenting the main results in Section 4. Finally, we highlight our main conclusions in Section 5.

2. Theoretical Background

Scalar–tensor theories with screening mechanisms provide a well-motivated framework to reconcile modifications of gravity on cosmological scales with stringent local constraints. Among them, the chameleon formalism [29] represents a prototypical example, in which the scalar degree of freedom dynamically adapts its mass to the surrounding environment, suppressing deviations from GR in high-density regions while remaining active on large scales.

The dynamics of a chameleon scalar field ϕ, conformally coupled to matter fields $\psi^{(i)}$, is described by the Einstein-frame Lagrangian

$$\mathcal{L} = \sqrt{-g}\left[-\frac{M_{\rm Pl}^2}{2}R + \frac{1}{2}(\partial\phi)^2 + V(\phi)\right] + \mathcal{L}_{\rm m}\left(\psi^{(i)}, g_{\mu\nu}^{(i)}\right), \tag{1}$$

where $M_{\rm Pl} = (8\pi G)^{-1/2}$ is the reduced Planck mass, and G is the gravitational constant. Matter fields follow geodesics of the Jordan-frame metric

$$g_{\mu\nu}^{(i)} = e^{-2Q_i\phi/(M_{\rm Pl}c^2)}\,\tilde{g}_{\mu\nu}, \tag{2}$$

with Q_i denoting the dimensionless coupling between the scalar field and the i-th matter species, and c being the speed of light. Throughout this work, we adopt a universal coupling Q for both baryonic and dark matter components, as commonly assumed in phenomenological analyses (e.g., [38,48]).

A particularly relevant case is provided by metric $f(R)$ theories of gravity, which can be recast as scalar–tensor models with a chameleon-like screening mechanism. In this correspondence, the scalar degree of freedom is identified with $f_R \equiv \partial f/\partial R$, and the coupling takes the fixed value $Q = 1/\sqrt{6}$ [49,50]. The connection between the chameleon field and the scalaron is given by the following equation (see, for example, [51]):

$$|f_R| = \exp\left(-\frac{2Q\phi}{M_{\rm Pl}c^2}\right) - 1\,, \tag{3}$$

where the quantity $\phi/M_{\rm Pl}$ carries the dimension of a gravitational potential. As a result, the formalism we develop below applies equally to generic chameleon models and to the class of viable $f(R)$ theories considered in this work.

The self-interaction of the scalar field is encoded in a monotonic potential, which can be described with an inverse power-law form (e.g., [52]),

$$V(\phi) = \lambda^{4+n}\,\phi^{-n}, \tag{4}$$

where $n > 0$ and λ set the characteristic energy scale, typically associated with the dark-energy scale [40,47].

In the quasi-static, non-relativistic regime relevant for galaxy clusters, the scalar field equation of motion reads

$$\nabla^2\phi = V'(\phi) + \frac{Q}{M_{\rm Pl}c^2}\sum_j \rho_j\, e^{Q\phi/(M_{\rm Pl}c^2)}, \tag{5}$$

where the sum runs over all matter components with density ρ_j. The coupling to matter gives rise to an effective potential,

$$V_{\rm eff}(\phi) = V(\phi) + \sum_j \rho_j\, e^{Q\phi/(M_{\rm Pl}c^2)}, \tag{6}$$

whose minimum depends explicitly on the ambient density. Since current observational constraints require $\phi/(M_{\rm Pl}c^2) \ll 1$ [36,53,54], the exponential term can be linearized, leading to

$$\nabla^2\phi \simeq \frac{Q}{M_{\rm Pl}c^2}\sum_j \rho_j + V'(\phi). \tag{7}$$

In this form, ϕ plays the role of an additional gravitational potential, mediating a fifth force, whose strength depends on the local density. In particular, assuming spherical symmetry, the total gravitational acceleration acting on non-relativistic tracers can be written as

$$\frac{{\rm d}\Phi}{{\rm d}r} = \frac{GM(r)}{r^2} + \frac{Q}{M_{\rm Pl}}\frac{{\rm d}\phi}{{\rm d}r}, \tag{8}$$

which motivates the definition of an effective mass associated with the scalar field,

$$M_{\rm eff}(r) = \frac{Q}{G}\frac{r^2}{M_{\rm Pl}}\frac{{\rm d}\phi}{{\rm d}r}. \tag{9}$$

The total dynamical mass inferred from kinematic probes is therefore

$$M_{\rm dyn}(r) = M_{\rm GR}(r) + M_{\rm eff}(r)\,, \tag{10}$$

where $M_{\rm GR}(r)$ is the total mass profile sourced by the matter components ρ_j.

An important feature of chameleon and $f(R)$ gravity is that null geodesics are invariant under conformal transformations. As a consequence, gravitational lensing remains sensitive only to the Newtonian potential generated by $M_{\rm GR}$ [31]. Lensing observations, thus, provide an independent and (ideally) unbiased probe of the true mass distribution, which we exploit as a prior in our analysis.

Semi-Analytical Solutions for the Chameleon Field

The chameleon mechanism naturally divides the phenomenology into two regimes. Deep inside a massive object, where the density is high, the field rapidly relaxes to the minimum of $V_{\rm eff}$ and spatial gradients become negligible. In this screened region, the scalar field approximately satisfies

$$\phi_{\rm int} \simeq \left(\frac{Q\,\rho_{\rm tot}}{n\,\lambda^{4+n}M_{\rm Pl}}\right)^{-1/(n+1)}, \tag{11}$$

with $\rho_{\rm tot} = \sum_j \rho_j$. As a consequence, the fifth force is strongly suppressed and gravity effectively reduces to GR. In the following, as usually done [47,55], we will assume $\phi_{\rm int} \sim 0$.

At larger radii, where the matter density decreases and the field has not yet settled to the minimum of the effective potential, the contribution of $V'(\phi)$ becomes subdominant. In this unscreened regime, the scalar field obeys

$$\nabla^2\phi_{\rm out} \simeq \frac{Q}{M_{\rm Pl}}\,\rho_{\rm tot}. \tag{12}$$

Assuming spherical symmetry, which is a good approximation for relaxed galaxy clusters [56,57], this equation reduces to

$$\frac{1}{r^2}\frac{\rm d}{{\rm d}r}\left(r^2\frac{{\rm d}\phi_{\rm out}}{{\rm d}r}\right) = \frac{Q}{M_{\rm Pl}}\,\rho_{\rm tot}(r). \tag{13}$$

A single integration shows explicitly that the scalar-field gradient, and hence the fifth force, is sourced by the enclosed mass profile

$$r^2 \frac{\mathrm{d}\phi_{\rm out}}{\mathrm{d}r} = \frac{Q}{M_{\rm Pl}} \int_0^r r'^2 \rho_{\rm tot}(r)\, \mathrm{d}r' + C_{\rm s}, \tag{14}$$

where $C_{\rm s}$ is an integration constant. The full scalar-field profile is obtained by matching the interior and exterior solutions at a characteristic screening radius $r = S$, defined as the scale at which the transition between the screened and unscreened regimes occurs (e.g., [58,59]). Imposing a continuity of ϕ and its derivative at $r = S$ uniquely fixes the integration constant in Equation (14).

Within $r < S$, the field is strongly suppressed, $\phi \ll \phi_\infty$, and the fifth force is negligible, whereas at $r > S$ the scalar field mediates a long-range modification of gravity. This screening radius therefore encapsulates the environmental dependence of chameleon and $f(R)$ gravity and plays a central role in the phenomenology of galaxy clusters.

Indeed, as already pointed out in [47,60], Equation (14) depends on the profile assumed to model the matter density distribution, impacting the shape of the chameleon field profile and changing the efficiency of the screening mechanism. The analysis carried out by [47] on simulated cluster-sized halos further demonstrates that the effect of mass modeling does not introduce relevant biases or spurious detections in the constrained parameter space, when other systematics are under control. However, this may be not the case for real clusters, where observational systematics and assumptions in the mass reconstruction are expected to affect the analysis [61].

In this work, we follow the approach of [61] and we consider three mass profile ansätze, which have found to provide adequate fit to the total matter distributions in observed clusters [24,62], namely the Navarro–Frenk–White (NFW) model [63],

$$M_{\rm NFW}(r) = M_{200} \frac{\ln(1 + r/r_{\rm s}) - \frac{r/r_{\rm s}}{(1+r/r_{\rm s})}}{\ln(1 + r_{200}/r_{\rm s}) - \frac{r_{200}/r_{\rm s}}{(1+r_{200}/r_{\rm s})}}, \tag{15}$$

where $r_{\rm s} \equiv r_{-2}$ is the radius at which the logarithmic derivative of the density profile assumes a value of -2; the Burkert model (e.g., Ref. [64]), is defined as

$$M_{\rm Bur}(r) = M_{200} \frac{\ln\left[1 + (r/r_{\rm s})^2\right] + 2\ln(1 + r/r_{\rm s}) - 2\arctan(r/r_{\rm s})}{\ln\left[1 + (r_{200}/r_{\rm s})^2\right] + 2\ln(1 + r_{200}/r_{\rm s}) - 2\arctan(r_{200}/r_{\rm s})}, \tag{16}$$

where $r_{\rm s} \simeq 2/3\, r_{-2}$, and, finally, the Hernquist profile (e.g., Ref. [65]),

$$M_{\rm Her}(r) = M_{200} \frac{(r_{200} + r_{\rm s})^2}{r_{200}^2} \frac{r^2}{(r + r_{\rm s})^2}, \tag{17}$$

with $r_{\rm s} = 2\, r_{-2}$. All profiles are characterized by two free parameters, the scale radius and the "virial" radius r_{200}, defined as the radius of a sphere enclosing an average density 200 times the critical density of the universe at the cluster's redshift. The corresponding virial mass is $M_{200} = M(r_{200})$.

Each model exhibits a different behavior at small and large scales; for $r \to 0$ the Burkert profile flattens, while the NFW and Hernquist models diverges as r^{-1}. As r grows, the Hernquist density decreases as $\sim r^{-4}$, faster than the other two ($\propto r^{-3}$).

Consequently, this translates to a distinct shape for the external gradient in the last term in the RHS of Equation (8). More specifically, for the NFW model, one has

$$\frac{\mathrm{d}\phi_{\rm out}}{\mathrm{d}r} = \frac{\mathcal{B}}{r_{\rm s}\, x^2} \left[\frac{1}{x+1} + \ln(x+1)\right] + \frac{C_{\rm s}}{r_{\rm s}\, x^2}, \tag{18}$$

where $x = r/r_s$, $\mathcal{B} = \mathcal{Q}\rho_s r_s^2/M_{\rm Pl}$, C_s is the integration constant defined above and $\rho_s(r_s, r_{200})$ is the typical central density parameter. The conditions at the matching radius, $x_c = S/r_s$, are given by

$$x_c = \left[\frac{\mathcal{B}}{\phi_\infty} - 1\right], \quad C_s = -\phi_\infty - \mathcal{B}\ln\left(\frac{\mathcal{B}}{\phi_\infty}\right). \tag{19}$$

Above, the quantity ϕ_∞ represents the value of the field in the background and it is one of the free parameters we aim to constrain. The exterior chameleon field gradient in the case of a Burkert profile is given by

$$\frac{d\phi_{\rm out}}{dr} = \frac{C_s}{r_s\, x^2} + \frac{\mathcal{B}}{r_s\, x^2}\left[\frac{1}{4}\ln\left(x^2+1\right) + \frac{1}{2}\ln(x+1) - \frac{1}{2}\tan^{-1}(x)\right], \tag{20}$$

and the matching with the inner solution is obtained when

$$C_s = \frac{1}{4}\left[-2\mathcal{B}\log\left(x_c^2+1\right) + \pi\mathcal{B} - 4\phi_\infty\right].$$

To get the screening radius S, one has to solve the numerical equation

$$\ln\left[\frac{x_c^2+1}{(x_c+1)^2}\right] + 2\tan^{-1}(x_c) = \pi - 4\frac{\phi_\infty}{\mathcal{B}}, \tag{21}$$

As for the Hernquist model, the gradient reads

$$\frac{d\phi_{\rm out}}{dr} = \frac{(x+1)^{-2}(x-3x-1)}{2\,x^2}\mathcal{B} + \frac{C_s}{r_s x^2}, \tag{22}$$

with the conditions

$$\begin{aligned} x_c &= \left(\frac{2\phi_\infty}{\mathcal{B}}\right)^{-\frac{1}{2}} - 1, \\ C_s &= \frac{(1 - x_c + 3\,x_c)}{2(1+x_c)^2}\mathcal{B}. \end{aligned} \tag{23}$$

3. Cluster Dataset and Analysis Set-Up

In this work we consider a sample of nine massive galaxy clusters from the CLASH [44] and CLASH-VLT [45] collaborations. The total CLASH sample includes 25 clusters for which high quality imaging data have been collected by the Hubble Space Telescope; 14 systems, accessible from the southern hemisphere, have been targeted by the spectroscopic follow up with the VIMOS instrument at the Very Large Telescope (VLT), providing a large amount—$\mathcal{O}(> 10^2)$—of confirmed spectroscopic cluster members with precise velocity determination.

Five of the CLASH clusters have been selected for their strong lensing features, while the other 20 systems have been chosen from Chandra observations for the high X-ray temperatures ($kT_X > 5$ keV) and morphologically regular shape. For a large subset of the CLASH sample—including the nine clusters targeted in this work—deep ground-based multi-band imaging was obtained and analyzed for detailed weak-lensing studies as part of the CLASH program, as presented in [62]. The unprecedented quality of the CLASH and CLASH-VLT dataset enabled accurate mass profile reconstructions using independent probes, e.g., [57,62,66,67]. Several multi-band analyses have further addressed the dynamical and morphological properties of the CLASH clusters, e.g., [68–73], which revealed complex features suggesting that some systems may be far from an equilibrium configuration.

A series of recent works [61,74,75] focused on a subsample of nine CLASH clusters—Abell 383 (A383), Abell 209 (A209), RX J2129.7 + 0005 (R2129), MS2137 − 2353 (MS2137), RXC J2248.7 − 4431 (R2248, also named Abell S1063), MACS J1931.8 − 2635 (M1931), MACS J1115.9 + 0129 (M1115), MACS J1206.2 − 0847 (M1206), and MACS J0329.7 − 0211 (M329)—spanning the redshift range $0.18 \leq z \leq 0.45$, to investigate dynamical properties of member galaxies and to further constrain generic signatures of departures from GR.

Here we exploit the same nine systems to reconstruct the total gravitational potential in chameleon gravity via the kinematics of the member galaxies, and to provide bounds on the background scalaron field f_{R0} in the $f(R)$ sub-case. For each cluster, we adopt an informative prior on the mass profile parameters r_{-2}, r_{200} which is based on the results of the combined strong- and weak-lensing analyses of [62] for all the parametric mass models discussed in Section 2. This step is fundamental to break the degeneracy arising between the fifth force in chameleon screening and the parameters describing the matter distribution (see e.g., [38]). The joint weak- and strong-lensing analysis of [62] was carried out with CLUMI code [76,77], a likelihood-based framework formulated in terms of azimuthally averaged radial profiles of lensing observables. In this approach, the projected mass distribution of each cluster is represented by a piecewise-defined, radially binned convergence profile. The analysis combines inner constraints from 16-band Hubble Space Telescope (HST) observations [78] with wide-field multiband imaging obtained primarily with Suprime-Cam on a Subaru Telescope [79]. By combining complementary lensing probes, this framework not only improves the precision of the mass reconstruction but also enables a better calibration of probe-dependent systematic effects.

Specifically, the mass reconstruction was based on a joint input data vector composed of two sets of measurements: (1) central enclosed aperture-mass constraints at four equally spaced integration radii (10–40 arcsec), derived from detailed strong-lensing and weak-shear modeling of the CLASH-HST data [78]; and (2) weak-lensing shear and magnification-bias measurements on larger scales, evaluated in 10 logarithmically spaced radial bins. For all profiles, the position of the brightest cluster galaxy was adopted as the cluster centre.

To rigorously account for uncertainties in the reconstructed convergence profile, ref. [62] used a full covariance matrix that includes four distinct contributions: (1) statistical observational errors from the joint likelihood analysis; (2) residual mass-sheet uncertainty; (3) cosmic-noise covariance of an uncorrelated large-scale structure projected along the line of sight; and (4) intrinsic variations in the projected cluster lensing signal, driven primarily by halo triaxiality and correlated substructures.

Using the binned convergence profile and its full covariance matrix for each cluster, the CLASH weak- and strong-lensing analysis derived the posterior distribution of the halo structural parameters for the NFW, Burkert, and Hernquist mass models. In the present work, we adopt the corresponding marginalized posterior distribution, denoted $P_{\rm lens}(r_{-2}, r_{200})$, as a robust, data-driven prior.

As for the kinematic data, we consider the projected phase-space (p.p.s. hereafter) of each cluster $(R_i, v_{z,i})$, where R_i is the projected position of the i-th member galaxy with respect to the cluster center, and $v_{z,i}$ is the line-of-sight (los) velocity measured in the rest frame of the cluster. The selection of cluster members was performed by [74] using the CLUster Membership in Phase Space (CLUMPS) method of [80].

We analyze the p.p.s using the MG-MAMPOSST code of [46], a version of the MAMPOSST algorithm of [81] which performs a kinematic determination of the mass profile of spherical self-gravitating systems under the assumption of dynamical equilibrium. The method is based on the Jeans equations and it further assumes a Gaussian shape for the three-dimensional velocity field. MG-MAMPOSST is equipped with general parameterizations of the gravitational potential describing a variety of dark matter, dark energy

and modified gravity models viable at cosmological scales [57,82]. Note that solving the Jeans equations requires knowledge of the number density distribution of the galaxies, $\nu(r)$, and of the orbits' anisotropy profiles , defined as

$$\beta = 1 - \frac{\sigma_\theta^2 + \sigma_\phi^2}{2\sigma_r^2}, \tag{24}$$

where $\sigma_r^2, \sigma_\theta^2, and \sigma_\phi^2$ are the velocity dispersions along the radial, tangential, and azimuthal components respectively; in spherical symmetry, $\sigma_\theta^2 = \sigma_\phi^2$. The velocity anisotropy defines the average shapes of the orbits of galaxies in clusters, and it is generally a function of the distance from the cluster center.

$\beta(r)$ cannot be observed directly due to the so-called mass-anisotropy degeneracy (e.g., [83]); MG-MAMPOSST overcomes this limitation by assuming a parametric model for the anisotropy and fitting the parameters describing $\beta(r)$ along with those of the gravitational potential. We use the generalized Tiret model (e.g., [74,84,85]),

$$\beta_{gT}(r) = \beta_0 + (\beta_\infty - \beta_0)\frac{r}{r + r_\beta}, \tag{25}$$

which has been shown to provide a good description for a large variety of galaxy orbits in clusters [85]. In Equation (25), β_0 and β_∞ represent the anisotropy at $r = 0$ and at very large radii, while r_β is a scale radius and is usually set to be equal to r_{-2} of the cluster mass profile [24,66].

As for the number density profile, we rely on the results of [74], who fitted the projected distribution $N(R)$ of the member galaxies, correcting for completeness, adopting the method of [86]. All clusters' projected number density profiles are well-described by the projected NFW model, except for A209, for which the King model [87] is favored. While both models are described by two free parameters, in the Jeans equations, the normalization of $\nu(r)$ simplifies it, and the only parameter left is the characteristic scale radius r_ν. In the MG-MAMPOSST analysis, we consider a Gaussian prior on r_ν whose amplitude is set by the uncertainties found by the fit of [74]. A summary of the clusters' dynamical properties and the constraints on the mass profile parameters derived from lensing and kinematic analyses (in standard gravity), and on the number density scale radius can be found in Table 1 of [61].

Here we apply the same setup described in [61] and we consider galaxies within the projected region $R \in [0.05\,\mathrm{Mpc}, r_{200}^L]$, where r_{200}^L is the value of the virial radius estimated by the lensing analysis of Ref. [71]. As a consistency check, we varied the upper bounds by $\sim$10% for each cluster to ensure the final results are not significantly affected by this assumption.

We implement the expression of the gravitational potential of Equation (8), assuming the field profiles of Equations (18), (19) and (22) for the NFW, Burkert and Hernquist models respectively. For the general chameleon framework, the magnitude of departures from GR is entirely specified by the coupling constant $\mathcal{Q}$ and the background field value ϕ_∞. However, as discussed in Section 2, the shape of the fifth force also depends on the mass profile parameters. We thus perform a Monte Carlo-Markov Chain (MCMC) exploration of the full parameter space $(r_{200}, r_s, \beta_0, \beta_\infty, r_\nu, \mathcal{Q}, \phi_\infty)$. At each trial, we sample r_{200}, r_s from the lensing distribution, while assuming flat priors on β_0, β_∞. Note that, in MG-MAMPOSST, the scaled parameters $\mathcal{A}_{0,\infty} = 1/\sqrt{1 - \beta_{0,\infty}}$ are used for the anisotropy, which are always positive and < 1, $= 1$, and > 1 for tangential, isotropic, and radial orbits, respectively. We consider $\mathcal{A}_{0,\infty} \in [0.4, 7]$; the scale radius is instead sampled from an informative Gaussian distribution as described above. As for the chameleon parameters, we consider the rescaled variables (e.g., [38,54]), $\mathcal{Q}_2 = \mathcal{Q}/(1 + \mathcal{Q})$ and $\phi_2 = 1 - \exp[\phi/(10^4\, M_{\rm Pl})]$, which are

in the range $[0,1]$. When focusing on the $f(R)$ class, we instead assume a flat prior in $\log_{10} f_R \in [-8,3]$. For all the MCMC runs, we discard the first 5000 points as burn-in, and we ensure convergence by performing a Geller–Rubin test as detailed in [61].

4. Results

We first consider a general chameleon scenario. In Figure 1 we show, as an illustrative example, the allowed regions at $1\,\sigma$ (darker shaded areas) and $2\,\sigma$ (lighter shaded areas) in the $\mathcal{Q}_2, \phi_2$ plane obtained from the joint lensing and kinematical analysis of A209. Each panel corresponds to a different assumption for the total cluster mass distribution.

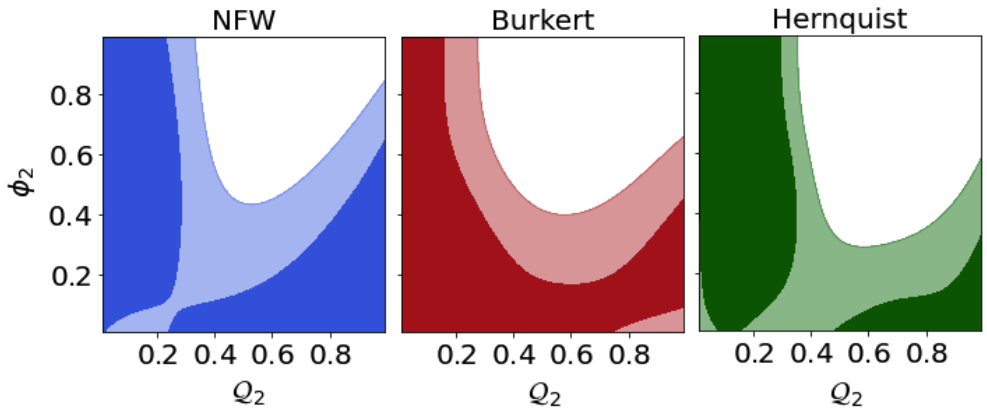

Figure 1. Two-dimensional allowed regions at 1σ (darker areas) and 2σ (lighter areas) in the $\mathcal{Q}_2, \phi_2$ plane from the MG-MAMPOSST analysis of A209. (**Left**): NFW mass profile. (**Center**): Burkert profile. (**Right**): Hernquist profile.

All the three posterior distributions in Figure 1 remain in agreement with the standard gravity expectation ($\mathcal{Q}_2 = \phi_2 = 0$) at the 2σ level; nevertheless, a marginal variation of the shape of the contours with the adopted mass profile can be observed in the regime of large deviations, $\mathcal{Q}_2 \gtrsim 0.6, \phi_2 \gtrsim 0.6$, where the excluded region slightly shrinks in the case of the NFW profile. This behavior reflects the different efficiency of the screening mechanism in clusters with distinct density slopes [47]. In particular, the NFW model exhibits a more efficient screening for large values of the coupling constant, generally leading to a larger allowed region in the parameter space, compared to the other two profiles. The full set of posterior distributions for all clusters is shown in Figures A1–A3 of Appendix A, corresponding to the NFW, Burkert, and Hernquist mass models, respectively.

When NFW or Hernquist profiles are assumed, no statistically significant ($\gtrsim 2\sigma$) deviation from GR is found for any cluster. A209 A383 and R2248 display mild ($\sim 1\sigma$) shifts away from $\mathcal{Q}_2 = 0$, $\phi_2 = 0$ when Hernquist is assumed, and M329 also when the NFW model is chosen, although three of these systems are known to present dynamical complexity. While the analysis of [73] revealed that M329 is not far from dynamical relaxation, the cluster resides in a relatively rich environment; R2248 shows signs of disturbance [61,72,82], and A209 exhibits evidence of a recent or ongoing merging event [70]. These factors may enhance degeneracies between dynamical mass parameters and modified-gravity degrees of freedom.

A slightly different behavior emerges when the cluster mass distribution is modeled with the Burkert profile. In this case, the tension in R2248 increases to the $\sim 3\sigma$ level, while A383, R2129 and M329 show a $\sim 1\sigma$ preference for larger chameleon parameters. This trend is consistent with the strong+weak lensing analyses of [62], which slightly disfavor the Burkert model relative to cuspy profiles for our cluster sample. In particular, for R2248 and

R2129 the lensing data better adapt to significantly smaller values of r_{200} and r_s than those inferred from kinematics in GR (see Figure 8 of [61]).

Within the chameleon framework, part of this tension can be absorbed by the additional parameters $\mathcal{Q}$ and ϕ_∞. Owing to the structure of Equation (6), the projected phase-space distribution of member galaxies can remain nearly unchanged if one compares a deeper potential well in GR (larger r_{200}) with a shallower mass profile supplemented by non-zero modified-gravity parameters. Consequently, when the lensing prior favors lower halo radii, the joint likelihood may shift probability toward parameter space regions associated with deviations from GR.

To quantify whether these shifts correspond to genuine support for modified gravity, we have further computed the Bayesian evidence $\ln Z$ for each mass-profile assumption in the joint kinematic+lensing analysis within the chameleon model. The values of $\ln Z$ are listed in Table 1 for all the nine clusters in the sample.

Table 1. Log-evidence ($\ln Z$) and differences with respect to the NFW model. Positive $\Delta \ln Z$ indicates preference over NFW.

Cluster	$\ln Z_{\rm NFW}$	$\ln Z_{\rm Hernquist}$	$\ln Z_{\rm Burkert}$	$\Delta \ln Z_{\rm Her}$	$\Delta \ln Z_{\rm Bur}$
A209	8091.010	8088.988	8084.830	−2.022	−6.180
A383	3771.540	3772.372	3770.583	0.831	−0.957
M1115	3303.020	3301.360	3302.977	−1.660	−0.043
M1206	3297.369	3297.727	3298.346	0.358	0.977
M1931	2035.744	2036.559	2034.657	0.815	−1.08
M329	1797.017	1798.084	1797.753	1.068	0.737
MS2137	1264.760	1264.028	1263.575	−0.732	−1.185
R2129	1467.501	1467.064	1465.270	−0.437	−2.231
R2248	6535.780	6536.338	6532.533	0.558	−3.247

It is worth to notice that the differences in log-evidence between NFW and Hernquist remain relatively small ($|\Delta \ln Z| \lesssim 1$–$2$), suggesting that the joint lensing and kinematic data do not significantly discriminate between these cuspy parameterizations once the modified-gravity sector is included. The Burkert profile is instead decisively disfavored in A209 ($\Delta \ln Z \simeq -6$ with respect to NFW), and moderately disfavored in R2248 ($\Delta \ln Z \gtrsim -3$) and R2129 ($\Delta \ln Z \gtrsim -2$).

The evidence under examination thus indicates that the mild shifts toward $\mathcal{Q}_2 > 0$ and $\phi_2 > 0$ observed in some Burkert-based runs may not be robust signatures of modified gravity, but rather manifestations of the degeneracy between mass-profile parameters and chameleon degrees of freedom under the adopted lensing priors. Kinematic-only runs assuming flat log-priors on r_{200} and r_s, and shows no preference of any model, with $\Delta \ln Z$ consistently smaller than 1. For completeness, we also evaluated the Akaike (AIC) and Bayesian (BIC) information criteria (see e.g., [85]), which are based on the comparison of the peak of the likelihoods and introduce penalties proportional to the number of free parameters. However, since all the mass models considered here share the same number of free parameters, these criteria reduce to a comparison based on the maximum likelihood, yielding results that are fully consistent with the Bayesian evidence.

Figure 2 further shows the posterior distribution of the screening radius S derived for each cluster assuming a NFW profile as a function of $(r_{200}, r_s, \phi_2, \mathcal{Q}_2)$. For six clusters out of nine, the distribution decreases by 90% above $S \sim 1$ Mpc, which is in agreement with the physical scale of galaxy clusters, while R2248, M1115 and M1931 exhibit a shallower posterior distribution at large S values.

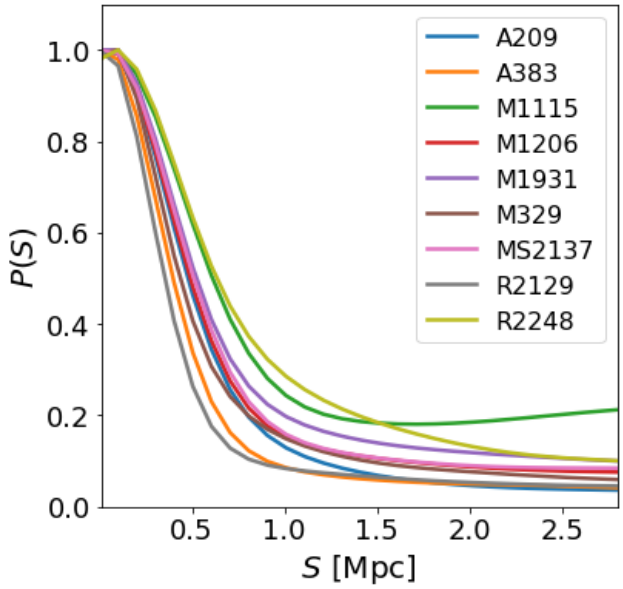

Figure 2. Posterior distributions of the screening radius S obtained from the analysis of the individual clusters. An NFW has been assumed to model the mass distribution.

In principle, the background chameleon field evolves with cosmological time (i.e.,: $\phi_\infty = \phi_\infty(z)$); this evolution is driven by the parameters characterizing the field potential (e.g., [31,88,89]); however, given the limited redshift range (0.19–0.45) spawned by our cluster sample, we can safely neglect the time evolution and combine the independent distributions of ϕ_2, $\mathcal{Q}_2$ of all clustera together. The joint two-dimensional constraints for ϕ_2 and $\mathcal{Q}_2$ are shown in Figure 3 for the three mass models.

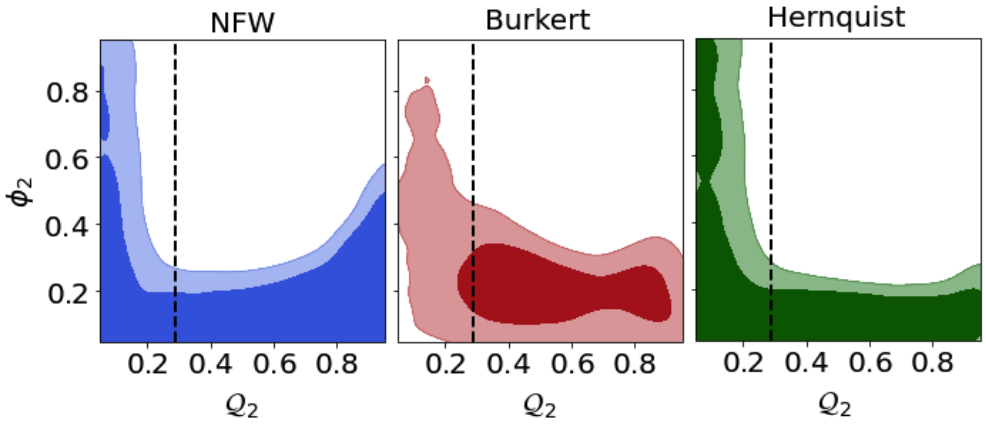

Figure 3. Two-dimensional 1σ (darker areas) and 2σ (lighter areas) allowed regions in the parameter space $\mathcal{Q}_2, \phi_2$ from the joint nine-clusters marginalized distribution. (**Left**): NFW. (**Central**): Burkert. (**Right**): Hernquist. The vertical dashed lines refer to $\mathcal{Q} = 1/\sqrt{6}$ (i.e., the sub-case of chameleon $f(R)$).

The NFW and Hernquist models show full agreement with GR, further providing strong bounds on the allowed parameter space, excluding the region $\phi_2, \mathcal{Q}_2 \gtrsim 0.4$. This confirms the forecasts of [46,47] and it results in the most stringent constraints on the general chameleon model at Mpc scale using galaxy clusters so far.

On the other hand, the Burkert model leads to a $\sim 2\sigma$ departure from the GR expectation in the combined analysis of all nine objects. This apparent tension originates from the slight cluster-by-cluster shifts in the posterior distribution towards $\phi_2, \mathcal{Q}_2 > 0$, which adds coherency to the joint constraint.

The $f(R)$ Sub-Case

As a second step, we consider the $f(R)$ class of chameleon models by fixing $\mathcal{Q} = 1/\sqrt{6}$ and identifying the scalaron field f_R as a function of the chameleon field ϕ according to Equation (3)[1]. We ran the MG-MAMPOSSt analysis again on all the clusters in our sample; the resulting one-dimensional distributions of $\log_{10}|f_R|$ are shown for NFW, Burkert and Hernquist in the three plots of Figure 4. In each panel we depict the single-cluster posteriors (solid lines with partial transparency) and the joint distribution obtained by combining the nine marginalized posteriors (solid line with full opacity).

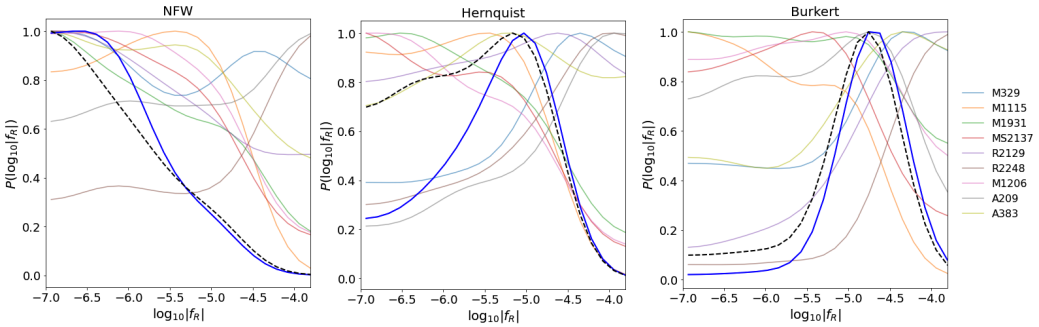

Figure 4. Marginalized distributions of the f_R background field from the MG-MAMPOSSt kinematic + lensing analysis of the nine clusters in our sample. (**Left**): NFW. (**Central**): Hernquist. (**Right**): Burkert. The solid blue lines correspond to the joint distributions obtained considering all the clusters, while the dashed black lines refer to the case where disturbed clusters are excluded.

Similarly to what found for the general chameleon framework, the joint posteriors for NFW and Hernquist mass models are in agreement with $|f_R| \to 0$, despite a slight $\sim 1\sigma$ shift in the latter case.

In Figure 5, we further show an example of the triangle plots for all the parameters involved in the analysis of A209 with the Hernquist profile. The shapes of the contours reflect the degeneracy among the scalaron field and the mass profile parameters r_{200}, r_s. In particular, the two-dimensional plane $r_{200} - \log_{10}|f_R|$ shows that the effect of the fifth force can be compensated by a shallower potential well (i.e., allowing for smaller r_{200}).

Overall, we obtain a joint constrain of $|f_R| \lesssim 2 \times 10^{-5}$ and $|f_R| \lesssim 5 \times 10^{-5}$ at 95% confidence limit for NFW and Hernquist, respectively.

As expected, the systematic tension with GR is more pronounced when adopting the Burkert profile, leading to a combined constraint of

$$\log_{10}|f_R| = -4.7 \pm 1.2, \tag{26}$$

which is in clear tension with current astrophysical and cosmological bounds (e.g., [40,90]).

To support the idea that this apparent deviation is driven by residual systematics rather than by genuine modified-gravity signatures, we follow the procedure outlined in [61] and restrict the joint analysis to dynamically relaxed systems. Specifically, we exclude clusters showing clear evidence of dynamical disturbance, as quantified by two complementary indicators: the fraction of galaxies in substructures, f_g, and the Anderson–Darling statistic A^2 computed from the line-of-sight velocity distribution of member galaxies.

The A^2 parameter measures departures from Gaussianity in the velocity distribution and has been shown to correlate strongly with the likelihood of spurious modified-gravity signals induced by non-equilibrium dynamics [91]. The fraction of galaxies in substructures, f_g, was estimated by [74] using the DS+ algorithm developed by [92], which exploits the full p.p.s. information to identify substructures. The corresponding values of A^2 and f_g are reported in the last two columns of Table 1 of [61], and we will not repeat them here.

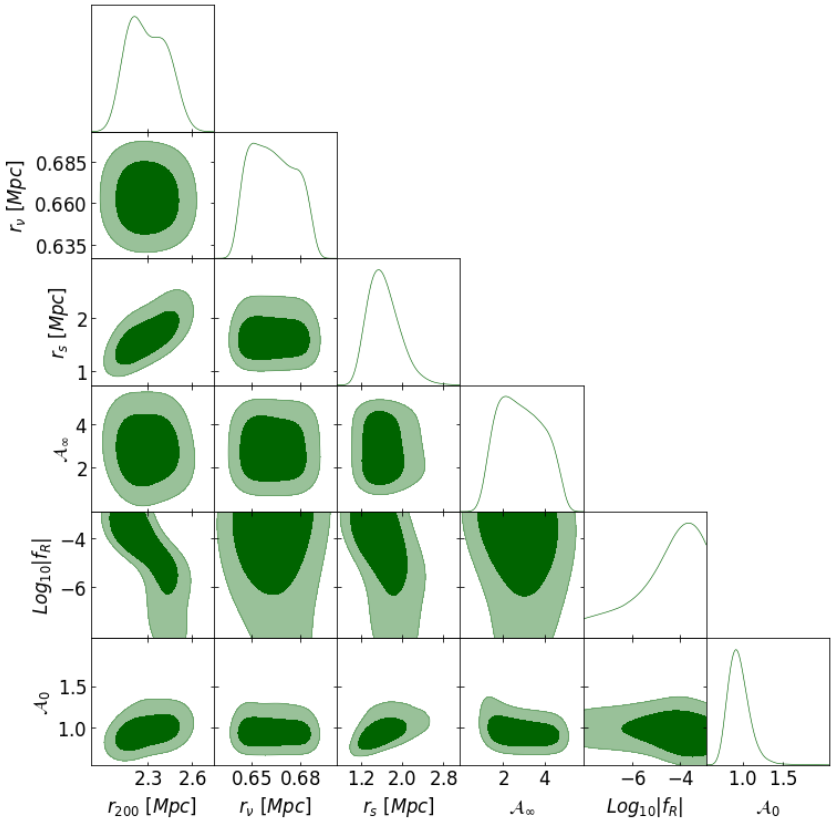

Figure 5. Marginalized one-dimensional (darker filled regions) and two-dimensional (lighter filled regions) distributions of free parameters in the MG-MAMPOSSt kinematic + lensing analysis of A209 in $f(R)$ gravity. The Hernquist model has been assumed for the total mass profile.

Note that selecting clusters with low values of A^2 and f_g does not only isolate dynamically relaxed systems, but also indirectly favors systems with a more regular and symmetric mass distribution. Indeed, relaxed clusters are expected to be closer to spherical symmetry, while strongly disturbed systems are more likely to exhibit significant triaxiality and projection effects.

This consideration is further supported by the properties of the CLASH sample itself, which has been shown from dedicated cosmological hydrodynamical simulations to not exhibit a significant orientation bias [93], making the use of spherical models a reasonable approximation at the level of precision considered here. Therefore, this selection partially mitigates potential systematics associated with departures from spherical symmetry. It is also important to point out that triaxiality is already considered as a source of statistical uncertainties in the strong+weak lensing covariance matrices, calibrated on numerical simulations [62,79].

We remove from the joint fit the systems with $f_g > 0.3$ and $A^2 > 0.7$, namely A209, M1115, R2248 and MS2137; the resulting distributions are shown as the black dashed lines in Figure 4. While the upper limits are almost unchanged, a rise in the marginalized distribution at $|f_R| \to 0$ is found in all the cases, most notably for the Hernquist mass model. This exercise stresses once again the importance of systematic calibration and accurate mass modeling when using cluster mass profiles to test the nature of gravity. The fact that our MG constraints remain stable when restricting the analysis to this sub-sample suggests that residual triaxiality is not the dominant driver of the observed trends, and that the main systematic effects are instead related to dynamical non-equilibrium.

5. Conclusions

In this work we have performed a joint kinematic–lensing test of chameleon screening gravity, and of its $f(R)$ sub-class, using nine massive galaxy clusters drawn from the CLASH and CLASH-VLT datasets. We modeled the dynamics of member galaxies with the MG-MAMPOSST code under the assumptions of spherical symmetry and dynamical equilibrium, and we adopted informative priors on the halo structural parameters (r_{200}, r_s) from strong+weak lensing reconstructions [62] (as implemented in [61]).

For the general chameleon scenario, we explored the parameter space $(\mathcal{Q}, \phi_\infty)$ adopting three alternative ansätze for the total mass distribution (NFW, Burkert, and Hernquist). When cuspy mass profiles are assumed (NFW or Hernquist), the combined nine-cluster constraints are consistent with GR and exclude large regions of the $(\mathcal{Q}_2, \phi_2)$ plane, roughly ruling out $\mathcal{Q}_2, \phi_2 \gtrsim 0.4$ at high credibility. These results are broadly consistent with expectations from previous cluster-scale forecasts [46,47] and analyses of real samples [38,54,58] and show that joint lensing–dynamics investigations can deliver stringent constraints on screened modifications of gravity at Mpc scales.

A different behavior emerges when adopting a Burkert profile for the total mass distribution. In this case, the cluster-by-cluster posteriors exhibit mild coherent shifts toward $\mathcal{Q}_2 > 0$ and $\phi_2 > 0$, which add up in the combined constraint and yield an apparent $\sim 2\sigma$ departure from the GR expectation. The evidence analysis indicates that these shifts do not constitute robust support for modified gravity, but are more naturally interpreted as a manifestation of the increased degeneracy between the modified-gravity sector and the mass-profile parameters when the assumed inner slope is in tension with the lensing constraints for part of the sample.

We then focused on the $f(R)$ sub-case by fixing $\mathcal{Q} = 1/\sqrt{6}$ and sampling the logarithm of the scalaron field $\log_{10}|f_R|$ with a flat, uninformative prior. For NFW and Hernquist, we find joint constraints consistent with $|f_R| \to 0$, and we obtain upper limits at the level of $|f_R| \lesssim 2 - 5 \times 10^{-5}$ (95% C.L.), in agreement with current cosmological constraints. Conversely, assuming a Burkert profile leads to a combined posterior peak away from zero, $\log_{10}|f_R| = -4.7 \pm 1.2$, which is in tension with astrophysical and cosmological bounds (e.g., [40,90]).

We have explicitly investigated the role of systematics in the dynamical state of the clusters by repeating the analysis after excluding clusters that show clear indications of non-equilibrium, based on the substructure fraction f_g and the Anderson–Darling statistic A^2. This procedure led to a shift of the marginalized posteriors toward $|f_R| \to 0$ for all mass models, supporting the interpretation that part of the apparent Burkert-driven tension is induced by residual dynamical complexity of the systems. At the same time, this exercise should be regarded as a targeted (and intentionally conservative) mitigation strategy rather than as an exhaustive treatment of systematics: additional effects such as projection effects and baryonic feedback are known to influence lensing mass determinations [94,95], see also the review of [96]; furthermore, residual l.o.s. interlopers contamination and potential modeling limitations of simple two-parameter mass profiles may still affect the inference at a non-negligible level, demanding a more accurate, multi-component analysis (e.g., [57,60]). Finally, it has been shown that triaxiality—although not being the dominant sources of systematics—may boost the mass profile when observing clusters along the line of sight [91]. As concerns lensing analyses, if the sample of clusters suffers an orientation bias toward alignment with the line of sight, then assuming either spherical or elliptical profiles would still lead to a net bias in the mass estimates [71]. For this reason, a dedicated upcoming work is addressing the extension of our framework to triaxial configurations of the mass profiles.

Note that strengthening cluster-scale tests of gravity requires both a broadening of the statistical sample (i.e., more clusters) and a meticulous control of systematics through a

more comprehensive multi-probe approach. This will become increasingly feasible thanks to the combination of new-generation wide-field photometric surveys enabling precise weak-lensing mass measurements—such as *Euclid* [97], the Vera Rubin Observatory [98], and the Roman Space Telescope [99]—and dedicated spectroscopic follow-up programs aimed at measuring member-galaxy velocities for large cluster samples (e.g., DESI [100], 4MOST [101], or MOONS/VLT [102]). In addition, several cluster-dedicated programs are already providing high-quality, multi-wavelength mass reconstructions that are particularly well suited for gravity tests at halo scales. Examples include X-COP [103], CHEX-MATE [104], and HeCS/HeCS-SZ [105,106], which combine X-ray, Sunyaev–Zel'dovich, and optical spectroscopic data to deliver accurate determinations of thermodynamic and dynamical profiles from the cluster core to the outskirts. Extending joint lensing–kinematics analyses to $\mathcal{O}(10^2)$–$\mathcal{O}(10^3)$ systems will not only reduce statistical uncertainties, but will also enable stringent consistency tests across dynamical state, mass, redshift, and environment, thereby isolating (and potentially modeling) the dominant sources of residual systematics.

Finally, while chameleon screening and simple $f(R)$ parameterizations are nowadays very well constrained, they remain an important and well-defined theoretical laboratory of modified gravity at cluster scales, offering a valuable baseline for more complex scenarios (e.g., extended scalar–tensor models [107], environment-dependent couplings, or beyond-Horndeski [108–110]/degenerate higher-order theories [111,112]) in which the phenomenology at cluster scales may be richer. In this sense, the present analysis represents a methodological stepping stone toward more general tests of gravity with upcoming cluster datasets.

Author Contributions: Conceptualization, L.P.; methodology, L.P.; software, L.P.; validation, L.P., K.U. and A.B.; formal analysis, L.P.; investigation, L.P. and F.R.; resources, K.U. and A.B.; data curation, K.U.; writing—original draft, L.P.; writing—review and editing, L.P., F.R., K.U. and A.B.; supervision, L.P.; Project administration, L.P. All authors have read and agreed to the published version of the manuscript.

Funding: L.P. acknowledges the support by the Italian Ministry for Research and University (MUR) under Grant 'Progetto Dipartimenti di Eccellenza 2023-2027' (BiCoQ). K.U. acknowledges support from the National Science and Technology Council, Taiwan (grant NSTC 112-2112-M-001-027-MY3) and the Academia Sinica Investigator award (grant AS-IA-112-M04).

Data Availability Statement: Part of the data are already publicly available on the CLASH-VLT database. Kinematic data for some clusters analyzed here have not been published yet and they are available upon reasonable request from the CLASH/CLASH-VLT team.

Acknowledgments: The authors acknowledge the CLASH-VLT team and its PI P. Rosati for the dataset provided to carry out the present work. We also thank the anonymous referees for the valuable comments and suggestions which helped improving our work.

Conflicts of Interest: The authors declare no conflicts of interest.

Appendix A. Marginal Distributions for the General Chameleon Case

Figures A1–A3 show the two-dimensional marginalized distributions at 1σ and 2σ (darker and lighter shaded areas) for all the clusters in our sample. Each figure presents the results for a different mass model used to describe the cluster matter profile in the MG-MAMPOSST fit.

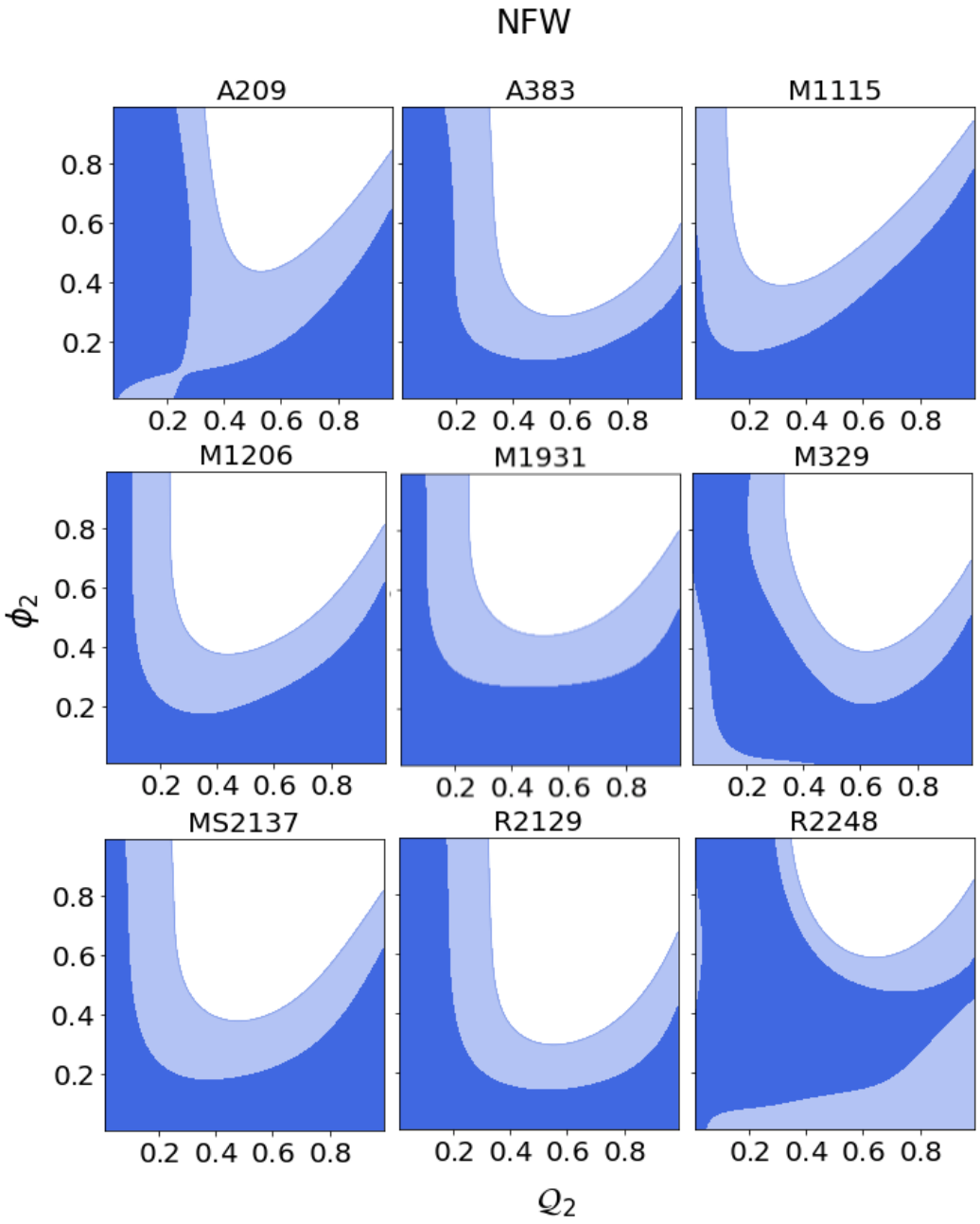

Figure A1. Two-dimensional 1σ (darker areas) and 2σ (lighter areas) allowed regions in the parameter space $\mathcal{Q}_2, \phi_2$ from the MG-MAMPOSSt kinematic + lensing analysis of the nine clusters in our sample. The NFW model has been assumed for the total matter distribution.

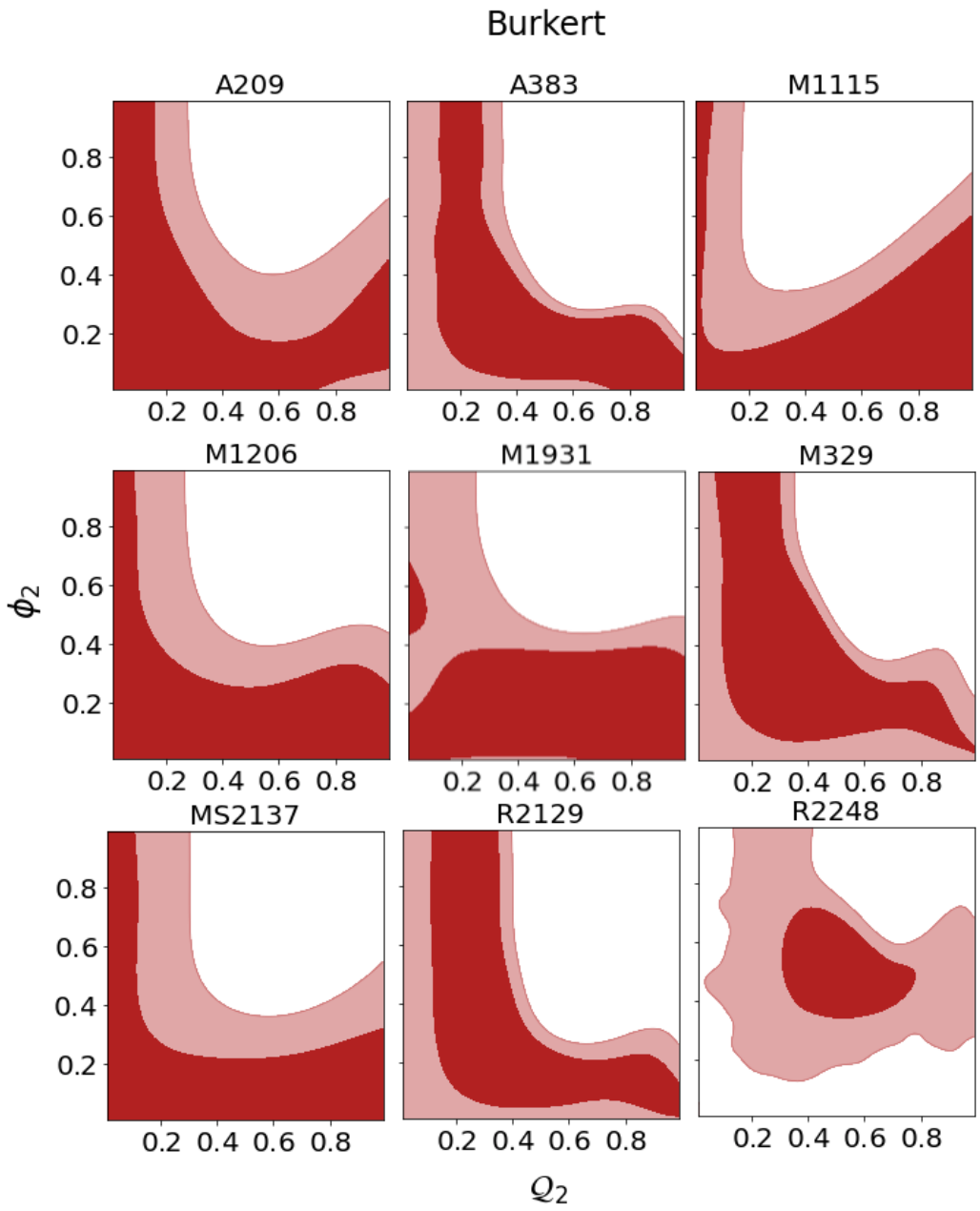

Figure A2. Same as Figure A1 but for the Burkert mass model.

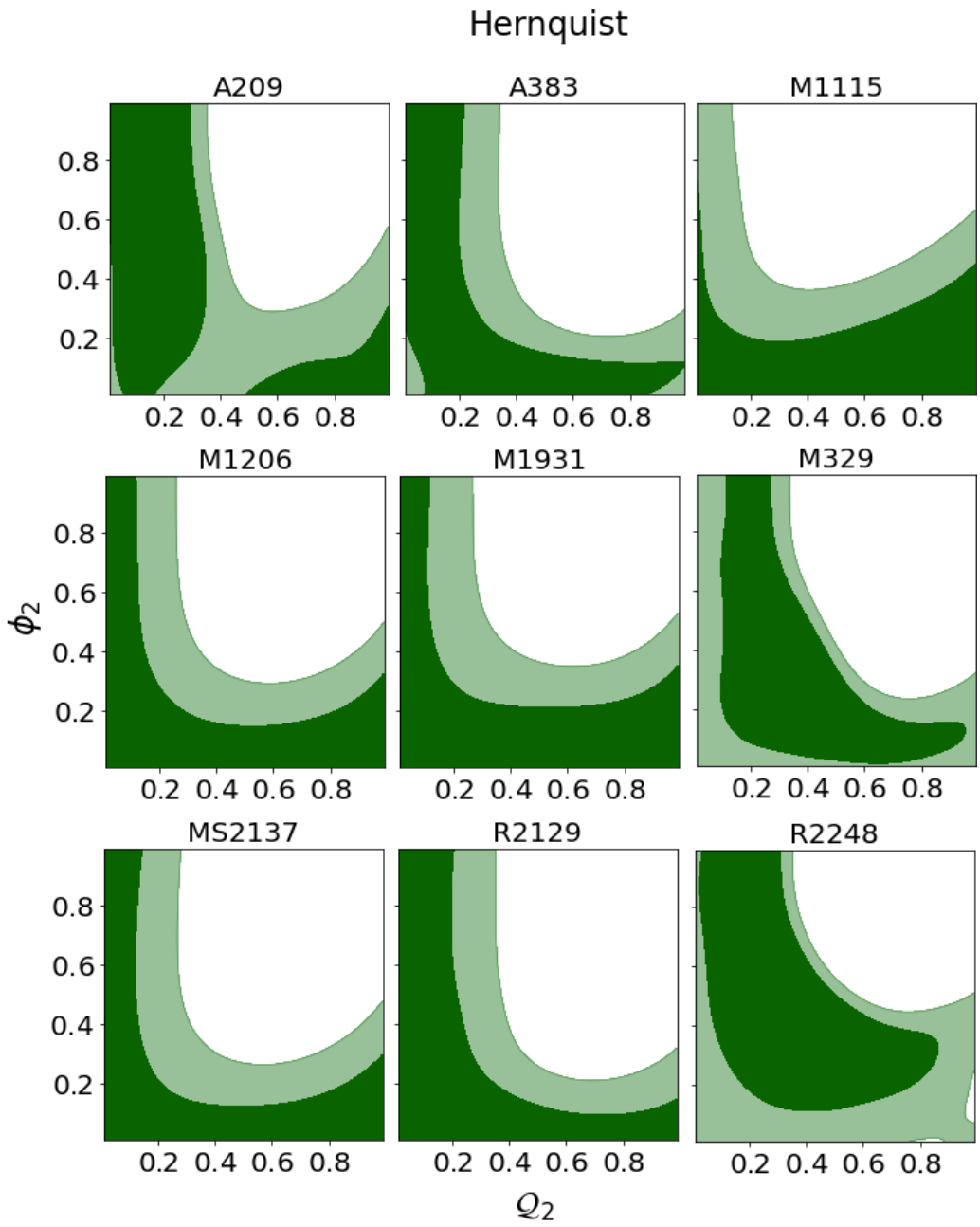

Figure A3. Same as Figure A1 but for the Hernquist mass model.

Notes

[1] To avoid excess notation, from now on, we indicate with f_R the background scalaron field.

References

1. Rubin, D.; Hayden, B. Is the Expansion of the Universe Accelerating? All Signs Point to Yes. *Astrophys. J. Lett.* **2016**, *833*, L30. [CrossRef]
2. Astier, P.; Pain, R. Observational evidence of the accelerated expansion of the universe. *Comptes Rendus Phys.* **2012**, *13*, 521–538. [CrossRef]
3. Martin, J. Everything you always wanted to know about the cosmological constant problem (but were afraid to ask). *Comptes Rendus Phys.* **2012**, *13*, 566–665. [CrossRef]
4. Padilla, A. Lectures on the Cosmological Constant Problem. *arXiv* **2015**, arXiv:1502.05296. . [CrossRef]
5. Aghanim, N. et al. [Planck Collaboration] Planck 2018 results. I. Overview and the cosmological legacy of Planck. *Astron. Astrophys.* **2020**, *641*, A1. [CrossRef]
6. *New Frontiers in Science in the Era of AI*; Springer Nature: Cham, Switzerland, 2024. [CrossRef]

7. Perivolaropoulos, L.; Skara, F. Challenges for ΛCDM: An update. *New Astron. Rev.* **2022**, *95*, 101659. [CrossRef]
8. Abbott, T. et al. [DES Collaboration] Dark Energy Survey Year 3 results: Cosmological constraints from galaxy clustering and weak lensing. *Phys. Rev. D* **2022**, *105*, 023520. [CrossRef]
9. Wang, D. The Self-Consistency of DESI Analysis and Comment on "Does DESI 2024 Confirm ΛCDM?". *arXiv* **2024**, arXiv:2404.13833. [CrossRef]
10. Ong, D.D.Y.; Yallup, D.; Handley, W. The Bayesian view of DESI DR2: Evidence and tension in a combined analysis with CMB and supernovae across cosmological models. *arXiv* **2026**, arXiv:2603.05472. [CrossRef]
11. Everitt, C.W.F. Experimental Tests of General Relativity: Past, Present and Future. In *Physics and Contemporary Needs: Volume 4*; Riazuddin, Ed.; Springer: Boston, MA, USA, 1980; pp. 529–555. [CrossRef]
12. Asmodelle, E. Tests of General Relativity: A Review. *arXiv* **2017**, arXiv:1705.04397. [CrossRef]
13. Ciufolini, I. The General Theory of Relativity and Its Tests in the Solar System. In *Recent Progress on Gravity Tests: Challenges and Future Perspectives*; Bambi, C., Cárdenas-Avendaño, A., Eds.; Springer Nature: Singapore, 2024; pp. 27–59. [CrossRef]
14. Koyama, K.; Sakstein, J. Astrophysical Probes of the Vainshtein Mechanism: Stars and Galaxies. *Phys. Rev. D* **2015**, *D91*, 124066. [CrossRef]
15. Saridakis, E.N.; Lazkoz, R.; Salzano, V.; Moniz, P.V.; Capozziello, S.; Jiménez, J.B.; De Laurentis, M.; Olmo, G.J. *Modified Gravity and Cosmology. An Update by the CANTATA Network*; Springer: Cham, Switzerland, 2021. [CrossRef]
16. Haggar, R.; Amoura, Y.; Mpetha, C.T.; Taylor, J.E.; Walker, K.; Power, C. Constraining Cosmological Parameters Using the Splashback Radius of Galaxy Clusters. *Astrophys. J.* **2024**, *972*, 28. [CrossRef]
17. Sakstein, J. Testing Gravity Using Dwarf Stars. *Phys. Rev. D* **2015**, *D92*, 124045. [CrossRef]
18. Pizzuti, L.; Sartoris, B.; Amendola, L.; Borgani, S.; Biviano, A.; Umetsu, K.; Mercurio, A.; Rosati, P.; Balestra, I.; Caminha, G.B.; et al. CLASH-VLT: Constraints on f(R) gravity models with galaxy clusters using lensing and kinematic analyses. *J. Cosmol. Astropart. Phys.* **2017**, *7*, 023. [CrossRef]
19. Artis, E.; Bulbul, E.; Grandis, S.; Ghirardini, V.; Clerc, N.; Seppi, R.; Comparat, J.; Cataneo, M.; von der Linden, A.; Bahar, Y.E.; et al. The SRG/eROSITA All-Sky Survey: Constraints on the structure growth from cluster number counts. *Astron. Astrophys.* **2025**, *696*, A5. [CrossRef]
20. Kravtsov, A.V.; Borgani, S. Formation of Galaxy Clusters. *Annu. Rev. Astron. Astrophys.* **2012**, *50*, 353–409. [CrossRef]
21. Gronke, M.; Llinares, C.; Mota, D.F.; Winther, H.A. Halo velocity profiles in screened modified gravity theories. *Mon. Not. R. Astron. Soc.* **2015**, *449*, 2837–2844. [CrossRef]
22. Bílek, M. Peculiar dark matter halos inferred from gravitational lensing as a manifestation of modified gravity. *Astron. Astrophys.* **2024**, *690*, A364. [CrossRef]
23. Hoekstra, H.; Bartelmann, M.; Dahle, H.; Israel, H.; Limousin, M.; Meneghetti, M. Masses of Galaxy Clusters from Gravitational Lensing. *Space Sci. Rev.* **2013**, *177*, 75–118. [CrossRef]
24. Biviano, A.; Rosati, P.; Balestra, I.; Mercurio, A.; Girardi, M.; Nonino, M.; Grillo, C.; Scodeggio, M.; Lemze, D.; Kelson, D.; et al. CLASH-VLT: The mass, velocity-anisotropy, and pseudo-phase-space density profiles of the z = 0.44 galaxy cluster MACS J1206.2-0847. *Astron. Astrophys.* **2013**, *558*, A1. [CrossRef]
25. Brax, P. Screening mechanisms in modified gravity. *Class. Quantum Gravity* **2013**, *30*, 214005. [CrossRef]
26. Koyama, K. Cosmological tests of modified gravity. *Rep. Prog. Phys.* **2016**, *79*, 046902. [CrossRef]
27. Brax, P.; Casas, S.; Desmond, H.; Elder, B. Testing Screened Modified Gravity. *Universe* **2021**, *8*, 11. [CrossRef]
28. Pizzuti, L. Testing Screening Mechanisms with Mass Profiles of Galaxy Clusters. *Universe* **2022**, *8*, 157. [CrossRef]
29. Khoury, J.; Weltman, A. Chameleon Fields: Awaiting Surprises for Tests of Gravity in Space. *Phys. Rev. Lett.* **2004**, *93*, 171104. [CrossRef]
30. Brax, P.; van de Bruck, C.; Davis, A.C.; Shaw, D. Dilaton and modified gravity. *Phys. Rev. D* **2010**, *82*, 063519. [CrossRef]
31. Burrage, C.; Copeland, E.J.; Moss, A.; Stevenson, J.A. The shape dependence of chameleon screening. *J. Cosmol. Astropart. Phys.* **2018**, *1*, 056. [CrossRef]
32. Bertolami, O.; Böhmer, C.G.; Harko, T.; Lobo, F.S.N. Extra force in f(R) modified theories of gravity. *Phys. Rev. D* **2007**, *75*, 104016. [CrossRef]
33. Fay, S.; Nesseris, S.; Perivolaropoulos, L. Can f(R) modified gravity theories mimic a ΛCDM cosmology? *Phys. Rev. D* **2007**, *76*, 063504. [CrossRef]
34. Burrage, C.; Sakstein, J. A compendium of chameleon constraints. *J. Cosmol. Astropart. Phys.* **2016**, *2016*, 045. [CrossRef]
35. Burrage, C.; Sakstein, J. Tests of chameleon gravity. *Living Rev. Relativ.* **2018**, *21*, 1. [CrossRef] [PubMed]
36. Desmond, H.; Ferreira, P.G. Galaxy morphology rules out astrophysically relevant Hu-Sawicki f (R) gravity. *Phys. Rev. D* **2020**, *102*, 104060. [CrossRef]
37. Benisty, D.; Brax, P.; Davis, A.C. Stringent pulsar timing bounds on light scalar couplings to matter. *Phys. Rev. D* **2023**, *107*, 064049. [CrossRef]

38. Wilcox, H.; Bacon, D.; Nichol, R.C.; Rooney, P.J.; Terukina, A.; Romer, A.K.; Koyama, K.; Zhao, G.; Hood, R.; Mann, R.G.; et al. The XMM Cluster Survey: Testing chameleon gravity using the profiles of clusters. *Mon. Not. Roy. Astron. Soc.* **2015**, *452*, 1171–1183. [CrossRef]
39. Cataneo, M.; Rapetti, D.; Lombriser, L.; Li, B. Cluster abundance in chameleonf(R) gravity I: Toward an accurate halo mass function prediction. *J. Cosmol. Astropart. Phys.* **2016**, *2016*, 024. [CrossRef]
40. Tamosiunas, A.; Briddon, C.; Burrage, C.; Cui, W.; Moss, A. Chameleon screening depends on the shape and structure of NFW halos. *J. Cosmol. Astropart. Phys.* **2022**, *2022*, 047. [CrossRef]
41. Jyoti, D.; Muñoz, J.B.; Caldwell, R.R.; Kamionkowski, M. Cosmic time slip: Testing gravity on supergalactic scales with strong-lensing time delays. *Phys. Rev. D* **2019**, *100*, 043031. [CrossRef]
42. Lian, Y.; Cao, S.; Liu, T.; Biesiada, M.; Zhu, Z.H. Direct Tests of General Relativity under Screening Effect with Galaxy-scale Strong Lensing Systems. *Astrophys. J.* **2022**, *941*, 16. [CrossRef]
43. Mu, C.; Cao, S.; Tian, S.; Jiang, X.; Zheng, C.; Cheng, D. Testing Screened Modified Gravity with Strongly Lensed Gravitational Waves. *arXiv* **2026**, arXiv:2603.09340. [CrossRef]
44. Postman, M.; Coe, D.; Benítez, N.; Bradley, L.; Broadhurst, T.; Donahue, M.; Ford, H.; Graur, O.; Graves, G.; Jouvel, S.; et al. The Cluster Lensing and Supernova Survey with Hubble: An Overview. *Astrophys. J. Suppl. Ser.* **2012**, *199*, 25. [CrossRef]
45. Rosati, P. et al. [Clash-VLT Team] CLASH-VLT: A VIMOS Large Programme to Map the Dark Matter Mass Distribution in Galaxy Clusters and Probe Distant Lensed Galaxies. *Messenger* **2014**, *158*, 48–53.
46. Pizzuti, L.; Saltas, I.D.; Amendola, L. MG-MAMPOSST: A code to test modifications of gravity with internal kinematics and lensing analyses of galaxy clusters. *Mon. Not. R. Astron. Soc.* **2021**, *506*, 595–612. [CrossRef]
47. Pizzuti, L.; Boumechta, Y.; Haridasu, S.; Pombo, A.M.; Dossena, S.; Butt, M.A.; Benetti, F.; Baccigalupi, C.; Lapi, A. Mass Modeling and Kinematics of Galaxy Clusters in Modified Gravity. *arXiv* **2024**, arXiv:2407.08778. [CrossRef]
48. Butt, M.A.; Haridasu, B.S.; Boumechta, Y.; Benetti, F.; Pizzuti, L.; Baccigalupi, C.; Lapi, A. Caustic and hydrostatic mass bias: Implications for modified gravity. *arXiv* **2024**, arXiv:2401.04698. [CrossRef]
49. Starobinsky, A.A. Disappearing cosmological constant in f (R) gravity. *JETP Lett.* **2007**, *86*, 157–163. [CrossRef]
50. Oyaizu, H.; Lima, M.; Hu, W. Nonlinear evolution of f (R) cosmologies. II. Power spectrum. *Phys. Rev. D* **2008**, *78*, 123524. [CrossRef]
51. Brax, P.; van de Bruck, C.; Davis, A.C.; Shaw, D.J. f(R) gravity and chameleon theories. *Phys. Rev. D* **2008**, *78*, 104021. [CrossRef]
52. Burrage, C.; Copeland, E.J.; Hinds, E. Probing dark energy with atom interferometry. *J. Cosmol. Astropart. Phys.* **2015**, *2015*, 042. [CrossRef]
53. Zhang, X.; Niu, R.; Zhao, W. Constraining the scalar-tensor gravity theories with and without screening mechanisms by combined observations. *Phys. Rev. D* **2019**, *100*, 024038. [CrossRef]
54. Boumechta, Y.; Haridasu, B.S.; Pizzuti, L.; Butt, M.A.; Baccigalupi, C.; Lapi, A. Constraining chameleon screening using galaxy cluster dynamics. *Phys. Rev. D* **2023**, *108*, 044007. [CrossRef]
55. Terukina, A.; Yamamoto, K. Gas Density Profile in Dark Matter Halo in Chameleon Cosmology. *Phys. Rev. D* **2012**, *86*, 103503. [CrossRef]
56. Laganá, T.F.; Durret, F.; Lopes, P.A.A. Physical properties of the X-ray gas as a dynamical diagnosis for galaxy clusters. *Mon. Not. R. Astron. Soc.* **2019**, *484*, 2807–2830. [CrossRef]
57. Biviano, A.; Pizzuti, L.; Mercurio, A.; Sartoris, B.; Rosati, P.; Ettori, S.; Girardi, M.; Grillo, C.; Caminha, G.B.; Nonino, M. CLASH-VLT: The Inner Slope of the MACS J1206.2-0847 Dark Matter Density Profile. *Astrophys. J.* **2023**, *958*, 148. [CrossRef]
58. Terukina, A.; Lombriser, L.; Yamamoto, K.; Bacon, D.; Koyama, K.; Nichol, R.C. Testing chameleon gravity with the Coma cluster. *J. Cosmol. Astropart. Phys.* **2014**, *4*, 013. [CrossRef]
59. Wilcox, H.; Nichol, R.C.; Zhao, G.B.; Bacon, D.; Koyama, K.; Romer, A.K. Simulation tests of galaxy cluster constraints on chameleon gravity. *Mon. Not. Roy. Astron. Soc.* **2016**, *462*, 715–725. [CrossRef]
60. Pizzuti, L.; Amatori, V.; Pombo, A.M.; Haridasu, S. The Shape of the Chameleon Fifth-Force on the Mass Components of Galaxy Clusters. *Universe* **2024**, *10*, 443. [CrossRef]
61. Pizzuti, L.; Biviano, A.; Umetsu, K.; Agostoni, E.; Autorino, A.; Pombo, A.M.; Mercurio, A.; D'Addona, M. CLASH-VLT: Constraining deviation from GR with the mass profiles of nine massive galaxy clusters. *arXiv* **2025**, arXiv:2509.16317. [CrossRef]
62. Umetsu, K.; Zitrin, A.; Gruen, D.; Merten, J.; Donahue, M.; Postman, M. CLASH: Joint Analysis of Strong-Lensing, Weak-Lensing Shear and Magnification Data for 20 Galaxy Clusters. *Astrophys. J.* **2016**, *821*, 116. [CrossRef]
63. Navarro, J.F.; Frenk, C.S.; White, S.D.M. The Structure of cold dark matter halos. *Astrophys. J.* **1996**, *462*, 563–575. [CrossRef]
64. Burkert, A. The Structure and evolution of weakly selfinteracting cold dark matter halos. *Astrophys. J. Lett.* **2000**, *534*, L143–L146. [CrossRef]
65. Hernquist, L. An Analytical Model for Spherical Galaxies and Bulges. *Astrophys. J.* **1990**, *356*, 359. [CrossRef]

66. Sartoris, B.; Biviano, A.; Rosati, P.; Mercurio, A.; Grillo, C.; Ettori, S.; Nonino, M.; Umetsu, K.; Bergamini, P.; Caminha, G.B.; et al. CLASH-VLT: A full dynamical reconstruction of the mass profile of Abell S1063 from 1 kpc out to the virial radius. *Astron. Astrophys.* **2020**, *637*, A34. [CrossRef]
67. Bergamini, P.; Grillo, C.; Rosati, P.; Vanzella, E.; Meštrić, U.; Mercurio, A.; Acebron, A.; Caminha, G.B.; Granata, G.; Meneghetti, M.; et al. A state-of-the-art strong-lensing model of MACS J0416.1-2403 with the largest sample of spectroscopic multiple images. *Astron. Astrophys.* **2023**, *674*, A79. [CrossRef]
68. Girardi, M.; Mercurio, A.; Balestra, I.; Nonino, M.; Biviano, A.; Grillo, C.; Rosati, P.; Annunziatella, M.; Demarco, R.; Fritz, A.; et al. CLASH-VLT: Substructure in the galaxy cluster MACS J1206.2-0847 from kinematics of galaxy populations. *Astron. Astrophys.* **2015**, *579*, A4. [CrossRef]
69. Donahue, M.; Ettori, S.; Rasia, E.; Sayers, J.; Zitrin, A.; Meneghetti, M.; Voit, G.M.; Golwala, S.; Czakon, N.; Yepes, G.; et al. The Morphologies and Alignments of Gas, Mass, and the Central Galaxies of Clash Clusters Of Galaxies. *Astrophys. J.* **2016**, *819*, 36. [CrossRef]
70. Jiménez-Teja, Y.; Dupke, R.; Benítez, N.; Koekemoer, A.M.; Zitrin, A.; Umetsu, K.; Ziegler, B.L.; Frye, B.L.; Ford, H.; Bouwens, R.J.; et al. Unveiling the Dynamical State of Massive Clusters through the ICL Fraction. *Astrophys. J.* **2018**, *857*, 79. [CrossRef]
71. Umetsu, K.; Sereno, M.; Tam, S.I.; Chiu, I.N.; Fan, Z.; Ettori, S.; Gruen, D.; Okumura, T.; Medezinski, E.; Donahue, M.; et al. The Projected Dark and Baryonic Ellipsoidal Structure of 20 CLASH Galaxy Clusters. *Astrophys. J.* **2018**, *860*, 104. [CrossRef]
72. Mercurio, A.; Rosati, P.; Biviano, A.; Annunziatella, M.; Girardi, M.; Sartoris, B.; Nonino, M.; Brescia, M.; Riccio, G.; Grillo, C.; et al. CLASH-VLT: Abell S1063: Cluster assembly history and spectroscopic catalogue. *Astron. Astrophys.* **2021**, *656*, A147. [CrossRef]
73. Girardi, M.; Boschin, W.; Mercurio, A.; Nocerino, N.; Nonino, M.; Rosati, P.; Biviano, A.; Demarco, R.; Grillo, C.; Sartoris, B.; et al. CLASH-VLT: Galaxy cluster MACS J0329–0211 and its surroundings using galaxies as kinematic tracers. *Astron. Astrophys.* **2024**, *692*, A175. [CrossRef]
74. Biviano, A.; Maraboli, E.A.; Pizzuti, L.; Rosati, P.; Mercurio, A.; De Lucia, G.; Ragone-Figueroa, C.; Grillo, C.; Granato, G.L.; Girardi, M.; et al. CLASH-VLT: The variance in the velocity anisotropy profiles of galaxy clusters. *Astron. Astrophys.* **2026**, *707*, A153. [CrossRef]
75. Maraboli, E.; Biviano, A.; Grillo, C.; Mercurio, A.; Pizzuti, L.; Rosati, P.; D'Addona, M. CLASH-VLT velocity anisotropy profiles in a stack of massive galaxy clusters. *arXiv* **2026**, arXiv:2602.15934. [CrossRef]
76. Umetsu, K.; Broadhurst, T.; Zitrin, A.; Medezinski, E.; Hsu, L.Y. Cluster Mass Profiles from a Bayesian Analysis of Weak-lensing Distortion and Magnification Measurements: Applications to Subaru Data. *Astrophys. J.* **2011**, *729*, 127. [CrossRef]
77. Umetsu, K. Model-free Multi-probe Lensing Reconstruction of Cluster Mass Profiles. *Astrophys. J.* **2013**, *769*, 13. [CrossRef]
78. Zitrin, A.; Fabris, A.; Merten, J.; Melchior, P.; Meneghetti, M.; Koekemoer, A.; Coe, D.; Maturi, M.; Bartelmann, M.; Postman, M.; et al. Hubble Space Telescope Combined Strong and Weak Lensing Analysis of the CLASH Sample: Mass and Magnification Models and Systematic Uncertainties. *Astrophys. J.* **2015**, *801*, 44. [CrossRef]
79. Umetsu, K.; Medezinski, E.; Nonino, M.; Merten, J.; Postman, M.; Meneghetti, M.; Donahue, M.; Czakon, N.; Molino, A.; Seitz, S.; et al. CLASH: Weak-lensing Shear-and-magnification Analysis of 20 Galaxy Clusters. *Astrophys. J.* **2014**, *795*, 163. [CrossRef]
80. Biviano, A.; van der Burg, R.F.J.; Balogh, M.L.; Munari, E.; Cooper, M.C.; De Lucia, G.; Demarco, R.; Jablonka, P.; Muzzin, A.; Nantais, J.; et al. The GOGREEN survey: Internal dynamics of clusters of galaxies at redshift 0.9–1.4. *Astron. Astrophys.* **2021**, *650*, A105. [CrossRef]
81. Mamon, G.A.; Biviano, A.; Boué, G. MAMPOSSt: Modelling Anisotropy and Mass Profiles of Observed Spherical Systems - I. Gaussian 3D velocities. *Mon. Not. R. Astron. Soc.* **2013**, *429*, 3079–3098. [CrossRef]
82. Pizzuti, L.; Saltas, I.D.; Umetsu, K.; Sartoris, B. Probing vainsthein-screening gravity with galaxy clusters using internal kinematics and strong and weak lensing. *Mon. Not. R. Astron. Soc.* **2022**, *512*, 4280–4290. [CrossRef]
83. Binney, J.; Mamon, G.A. M/L and velocity anisotropy from observations of spherical galaxies, or must M87 have a massive black hole? *Mon. Not. R. Astron. Soc.* **1982**, *200*, 361–375. [CrossRef]
84. Tiret, O.; Combes, F.; Angus, G.W.; Famaey, B.; Zhao, H.S. Velocity dispersion around ellipticals in MOND. *Astron. Astrophys.* **2007**, *476*, L1–L4. [CrossRef]
85. Mamon, G.A.; Cava, A.; Biviano, A.; Moretti, A.; Poggianti, B.; Bettoni, D. Structural and dynamical modeling of WINGS clusters. II. The orbital anisotropies of elliptical, spiral, and lenticular galaxies. *Astron. Astrophys.* **2019**, *631*, A131. [CrossRef]
86. Sarazin, C.L. A maximum likelihood method for determining the distribution of galaxies in clusters. *Astrophys. J.* **1980**, *236*, 75–83. [CrossRef]
87. King, I. The structure of star clusters. I. an empirical density law. *Astron. J.* **1962**, *67*, 471. [CrossRef] [PubMed]
88. Brax, P.; van de Bruck, C.; Davis, A.C.; Khoury, J.; Weltman, A. Detecting dark energy in orbit: The cosmological chameleon. *Phys. Rev. D* **2004**, *70*, 123518. [CrossRef]
89. Mota, D.F.; Schelpe, C.A.O. Evolution of the chameleon scalar field in the early universe. *Phys. Rev. D* **2012**, *86*, 123002. [CrossRef]
90. Bai, J.; Xia, J.Q.; Zhao, G.B. Testing f(R) Gravity from Cosmic Shear Measurements. *Astrophys. J.* **2025**, *992*, 205. [CrossRef]

91. Pizzuti, L.; Sartoris, B.; Borgani, S.; Biviano, A. Calibration of systematics in constraining modified gravity models with galaxy cluster mass profiles. *J. Cosmol. Astropart. Phys.* **2020**, *2020*, 024. [CrossRef]
92. Benavides, J.A.; Biviano, A.; Abadi, M.G. DS+: A method for the identification of cluster substructures. *Astron. Astrophys.* **2023**, *669*, A147. [CrossRef]
93. Meneghetti, M.; Rasia, E.; Vega, J.; Merten, J.; Postman, M.; Yepes, G.; Sembolini, F.; Donahue, M.; Ettori, S.; Umetsu, K.; et al. The Music of Clash: Predictions on the Concentration-Mass Relation. *Astrophys. J.* **2014**, *797*, 34. [CrossRef]
94. Grandis, S.; Bocquet, S.; Mohr, J.J.; Klein, M.; Dolag, K. Calibration of bias and scatter involved in cluster mass measurements using optical weak gravitational lensing. *Mon. Not. R. Astron. Soc.* **2021**, *507*, 5671–5689. [CrossRef]
95. Giocoli, C. et al. [Euclid Collaboration] Euclid preparation. XXXII. Evaluating the weak-lensing cluster mass biases using the Three Hundred Project hydrodynamical simulations. *Astron. Astrophys.* **2024**, *681*, A67. [CrossRef]
96. Umetsu, K. Cluster-galaxy weak lensing. *Astron. Astrophys. Rev.* **2020**, *28*, 7. [CrossRef]
97. Mellier, Y. et al. [Euclid Collaboration] Euclid: I. Overview of the Euclid mission. *Astron. Astrophys.* **2025**, *697*, A1. [CrossRef]
98. Ivezić, Ž.; Kahn, S.M.; Tyson, J.A.; Abel, B.; Acosta, E.; Allsman, R.; Alonso, D.; AlSayyad, Y.; Anderson, S.F.; Andrew, J.; et al. LSST: From Science Drivers to Reference Design and Anticipated Data Products. *Astrophys. J.* **2019**, *873*, 111. [CrossRef]
99. Sanderson, R.E.; Hickox, R.; Hirata, C.M.; Holman, M.J.; Lu, J.R.; Villar, A. Recommendations for Early Definition Science with the Nancy Grace Roman Space Telescope. *arXiv* **2024**, arXiv:2404.14342. [CrossRef]
100. Abareshi, B. et al. [DESI Collaboration] Overview of the Instrumentation for the Dark Energy Spectroscopic Instrument. *Astron. J.* **2022**, *164*, 207. [CrossRef]
101. De Jong, R.S.; Agertz, O.; Berbel, A.A.; Aird, J.; Alexander, D.A.; Amarsi, A.; Anders, F.; Andrae, R.; Ansarinejad, B.; Ansorge, W.; et al. 4MOST: Project overview and information for the First Call for Proposals. *Messenger* **2019**, *175*, 3–11. [CrossRef]
102. Cirasuolo, M.; Fairley, A.; Rees, P.; Gonzalez, O.A.; Taylor, W.; Maiolino, R.; Afonso, J.; Evans, C.; Flores, H.; Lilly, S.; et al. MOONS: The New Multi-Object Spectrograph for the VLT. *Messenger* **2020**, *180*, 10–17. [CrossRef]
103. Eckert, D.; Ettori, S.; Pointecouteau, E.; Molendi, S.; Paltani, S.; Tchernin, C. The XMM cluster outskirts project (X-COP). *Astron. Nachrichten* **2017**, *338*, 293–298. [CrossRef]
104. Arnaud, M. et al. [CHEX-MATE Collaboration] The Cluster HEritage project with XMM-Newton: Mass Assembly and Thermodynamics at the Endpoint of structure formation. I. Programme overview. *Astron. Astrophys.* **2021**, *650*, A104. [CrossRef]
105. Rines, K.; Geller, M.J.; Diaferio, A.; Kurtz, M.J. Measuring the Ultimate Halo Mass of Galaxy Clusters: Redshifts and Mass Profiles from the Hectospec Cluster Survey (HeCS). *Astrophys. J.* **2013**, *767*, 15. [CrossRef]
106. Rines, K.J.; Geller, M.J.; Diaferio, A.; Hwang, H.S. HeCS-SZ: The Hectospec Survey of Sunyaev–Zeldovich-Selected Clusters. *Astrophys. J.* **2016**, *819*, 63. [CrossRef]
107. Crisostomi, M.; Koyama, K.; Tasinato, G. Extended scalar-tensor theories of gravity. *J. Cosmol. Astropart. Phys.* **2016**, *2016*, 044. [CrossRef]
108. Kobayashi, T. Horndeski theory and beyond: A review. *Rep. Prog. Phys.* **2019**, *82*, 086901. [CrossRef]
109. Gleyzes, J.; Langlois, D.; Piazza, F.; Vernizzi, F. New Class of Consistent Scalar-Tensor Theories. *Phys. Rev. Lett.* **2015**, *114*, 211101. [CrossRef]
110. Zumalacárregui, M.; García-Bellido, J. Transforming gravity: From derivative couplings to matter to second-order scalar-tensor theories beyond the Horndeski Lagrangian. *Phys. Rev. D* **2014**, *89*, 064046. [CrossRef]
111. Langlois, D.; Mancarella, M.; Noui, K.; Vernizzi, F. Effective description of higher-order scalar-tensor theories. *J. Cosmol. Astropart. Phys.* **2017**, *2017*, 033. [CrossRef]
112. Langlois, D. Dark energy and modified gravity in degenerate higher-order scalar–tensor (DHOST) theories: A review. *Int. J. Mod. Phys. D* **2019**, *28*, 1942006. [CrossRef]